

TIRF microscopy with ultra-short penetration depth

Hao Shen,^{1,2} Eric Huang,² Tapaswini Das,³ Hongxing Xu,¹
Mark Ellisman,^{3,4} and Zhaowei Liu^{2,*}

¹*Institute of Physics, Chinese Academy of Sciences,
100190, Beijing, China*

²*Department of Electrical and Computer Engineering, University of California, San Diego,
9500 Gilman Drive, La Jolla, California 92093, USA*

³*National Center for Microscopy and Imaging Research, University of California, San Diego,
La Jolla, California 92093-0608, USA*

⁴*Department of Neurosciences, University of California San Diego,
La Jolla, California 92093-0608, USA*

[*zhaowei@ece.ucsd.edu](mailto:zhaowei@ece.ucsd.edu)

Abstract: Total internal reflection fluorescence microscopy (TIRF), in both commercial and custom-built configurations, is widely used for high signal-noise ratio imaging. The imaging depth of traditional TIRF is sensitive to the incident angle of the laser, and normally limited to around 100 nm. In our paper, using a high refractive index material and the evanescent waves of various waveguide modes, we propose a compact and tunable ultra-short decay length TIRF system, which can reach decay lengths as short as 19 nm, and demonstrate its application for imaging fluorescent dye-labeled F-actin in HeLa cells.

© 2014 Optical Society of America

OCIS codes: (110.0180) Microscopy; (180.2520) Fluorescence microscopy; (240.6690) Surface waves.

References and links

1. E. M. Slayter, *Optical Methods in Biology* (R. E. Krieger, 1976).
2. S. Kudo, Y. Magariyama, and S.-I. Aizawa, "Abrupt changes in flagellar rotation observed by laser dark-field microscopy," *Nature* **346**, 677–680 (1990).
3. J. B. Pawley, *Handbook of Biological Confocal Microscopy* (Springer, 1995).
4. T. Wilson, *Confocal Microscopy* (Academic, 1990).
5. M. Bates, B. Huang, G. T. Dempsey, and X. Zhuang, "Multicolor super-resolution imaging with photo-switchable fluorescent probes," *Science* **317**, 1749–1753 (2007).
6. M. J. Rust, M. Bates, and X. Zhuang, "Sub-diffraction-limit imaging by stochastic optical reconstruction microscopy (STORM)," *Nat. Methods* **3**, 793–796 (2006).
7. S. W. Hell and J. Wichmann, "Breaking the diffraction resolution limit by stimulated emission: stimulated-emission-depletion fluorescence microscopy," *Opt. Lett.* **19**, 780–782 (1994).
8. T. A. Klar and S. W. Hell, "Subdiffraction resolution in far-field fluorescence microscopy," *Opt. Lett.* **24**, 954–956 (1999).
9. B. Bailey, D. L. Farkas, D. L. Taylor, and F. Lanni, "Enhancement of axial resolution in fluorescence microscopy by standing-wave excitation," *Nature* **366**, 44–48 (1993).
10. M. G. L. Gustafsson, "Surpassing the lateral resolution limit by a factor of two using structured illumination microscopy," *J. Microsc.* **198**, 82–87 (2000).
11. F. Wei and Z. Liu, "Plasmonic structured illumination microscopy," *Nano Lett.* **10**, 2531–2536 (2010).
12. F. W. Rost, *Fluorescence Microscopy* (Cambridge University, 1995), Vol. 1–3.
13. T. Funatsu, Y. Harada, M. Tokunaga, K. Saito, and T. Yanagida, "Imaging of single fluorescent molecules and individual ATP turnovers by single myosin molecules in aqueous solution," *Nature* **374**, 555–559 (1995).

14. J. E. Hobbie, R. J. Daley, and S. Jasper, "Use of nucleopore filters for counting bacteria by fluorescence microscopy," *Appl. Environ. Microbiol.* **33**, 1225–1228 (1977).
15. R. Pepperkok and J. Ellenberg, "High-throughput fluorescence microscopy for systems biology," *Nat. Rev. Mol. Cell Biol.* **7**, 690–696 (2006).
16. J. M. Prober, G. L. Trainor, R. J. Dam, F. W. Hobbs, C. W. Robertson, R. J. Zagursky, A. J. Cocuzza, M. A. Jensen, and K. Baumeister, "A system for rapid DNA sequencing with fluorescent chain-terminating dideoxynucleotides," *Science* **238**, 336–341 (1987).
17. G. A. Wagnieres, W. M. Star, and B. C. Wilson, "In vivo fluorescence spectroscopy and imaging for oncological applications," *Photochem. Photobiol.* **68**, 603–632 (1998).
18. D. Axelrod, "Total internal reflection fluorescence microscopy," *Method. Cell Biol.* **89**, 169–221 (2008).
19. D. Axelrod, "Cell-substrate contacts illuminated by total internal-reflection fluorescence," *J. Cell Biol.* **89**, 141–145 (1981).
20. D. Breitsprecher, A. K. Kiesewetter, J. Linkner, and J. Faix, "Analysis of actin assembly by in vitro TIRF microscopy," in *Chemotaxis* (Springer, 2009), pp. 401–415.
21. B. Lassen and M. Malmsten, "Competitive protein adsorption studied with TIRF and ellipsometry," *J. Colloid Interface Sci.* **179**, 470–477 (1996).
22. M. Ohara-Imaizumi, C. Nishiwaki, T. Kikuta, S. Nagai, Y. Nakamichi, and S. Nagamatsu, "TIRF imaging of docking and fusion of single insulin granule motion in primary rat pancreatic beta-cells: different behaviour of granule motion between normal and Goto-Kakizaki diabetic rat beta-cells," *Biochem. J.* **381**, 13–18 (2004).
23. M. Tokunaga, K. Kitamura, K. Saito, A. H. Iwane, and T. Yanagida, "Single molecule imaging of fluorophores and enzymatic reactions achieved by objective-type total internal reflection fluorescence microscopy," *Biochem. Biophys. Res. Commun.* **235**, 47–53 (1997).
24. C. M. Ajo-Franklin, L. Kam, and S. G. Boxer, "High refractive index substrates for fluorescence microscopy of biological interfaces with high z contrast," *Proc. Natl. Acad. Sci. U. S. A.* **98**, 13643–13648 (2001).
25. D. S. Johnson, J. K. Jaiswal, and S. Simon, "Total internal reflection fluorescence (TIRF) microscopy illuminator for improved imaging of cell surface events," in *Current Protocols in Cytometry* (John Wiley, 2012).
26. L. Wang, C. Vasilev, D. P. Canniffe, L. R. Wilson, C. N. Hunter, and A. J. Cadby, "Highly confined surface imaging by solid immersion total internal reflection fluorescence microscopy," *Opt. Express* **20**, 3311–3324 (2012).

1. Introduction

Since its invention centuries ago, optical microscopy has become an irreplaceable tool in a wide variety of fields. Over the years, many advances have been developed to expand its limitations, particularly for biological applications and research. Some of these developments, such as dark field microscopy and phase contrast microscopy [1, 2], seek to increase the image contrast of an object. Others, like confocal microscopy [3, 4], STORM [5, 6] STED [7, 8], SIM [9, 10], and PSIM [11], aim to increase the effective resolution of the image. Of particular note are the techniques targeting fluorescence-labeled specimens [12], which have become incredibly useful ways to image biological samples [13–17]. Standard epi-fluorescence microscopy, where the entire sample is flooded with the excitation light, is commonly used for the imaging of tagged biological samples. Another fluorescence microscopy technique is Total Internal Reflection Fluorescence (TIRF) microscopy [18, 19], which uses the evanescent field produced by total internal reflection to achieve extremely thin optical sectioning as well as high signal-to-noise ratios.

Normally, total internal reflection occurs when light from a region with a high index of refraction is incident on a region of lower index and its angle of incidence is higher than the critical angle $\theta_c = \sin^{-1}(n_1/n_2)$, where n_1 and n_2 are respectively the lower and higher indices of refraction at the boundary. Although no light is radiated to the lower index medium, there exists an exponentially decaying evanescent wave on the far side of the interface. The power of this evanescent wave, which decays as $P = P_0 e^{-2kz}$ where z is the distance away from the surface and $k = \frac{\omega}{c} \sqrt{(n_2 \sin \theta_i)^2 - (n_1)^2}$ where θ_i is the angle of incidence, can excite any fluorophores that are exposed to this field. For example, a commercially available Carl Zeiss TIRF objective (Plan-Fluar 100x/1.45 Oil) can reach 75 nm penetration depth (532 nm laser @ maximum 72 degree) at the glass and water interface. As a result, TIRF microscopy can achieve very high contrast images near the interface [20–23]. This capability makes TIRF a very useful

imaging method, and there have recently been many proposed modifications for expanding its capabilities [24–26]. Here, we propose and experimentally demonstrate a thin film waveguide based compact TIRF method for achieving an ultra-short tunable decay length ranging from 19 nm to 39 nm.

2. Experiment and discussion

2.1. Working principles

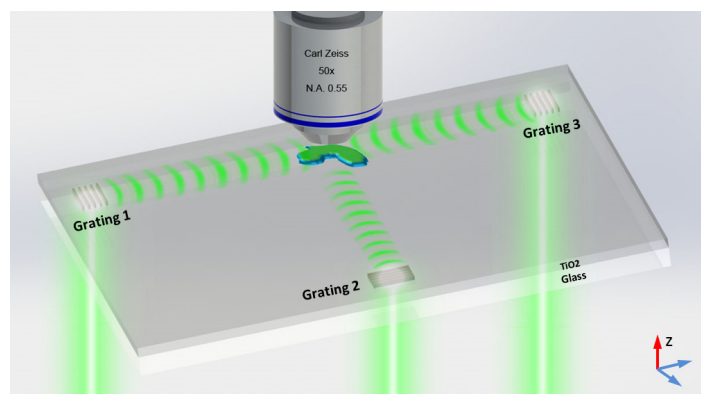


Fig. 1. Schematic of the proposed TIRF system. The TiO_2 layer acts as a waveguide capable of supporting a variety of propagating modes, each of which have a different wavelength. The gratings are all designed to couple to different modes when illuminated with a normally incident laser.

Our TIRF setup consists of a TiO_2 layer on a 22 by 22 mm glass coverslip, with several gratings fabricated 5 mm away from the central sample region (Fig. 1). The TiO_2 layer is able to support several waveguide modes, each with a unique decay length at the imaging surface. Although the evanescent fields from total internal reflection do not radiate into free space, they will excite the fluorescent particles near the surface. The gratings are used to selectively couple an incident laser into a specific waveguide mode. The waveguide modes from the gratings propagate to the sample, which fluoresces when exposed to the evanescent field. As a result, this configuration allows for the tuning of the decay length through the selection of the illuminated grating. Additionally, TiO_2 has a higher index of refraction ($n=2.5$) compared to glass ($n=1.47$), which results in a shortened decay length when compared to traditional TIRF experiments.

In order to design the parameters of the waveguide, we used a commercially available finite element solver (COMSOL Multiphysics 4.3a) to identify the propagating modes for given thickness of the waveguide layer, which should follow the relationship $N\lambda/2n_2 = d$, where the λ is wavelength of incident laser (532 nm for this experiment); the N is an integer and the d is the thickness of TiO_2 layer (Figs. 2(a) and 2(b)). The parameter of interest is $\alpha = k_x/k_0$, which affects the penetration depth of the electric field through the formula $z = (2 \times k_0 \times \sqrt{(\alpha^2 - 1)})^{-1}$ where $k_0 = 2\pi/\lambda$. After selecting a TiO_2 thickness of 1 μm , we then identified three modes with different values of k_x/k_0 (highlighted in Fig. 2(a)), and designed our three gratings with different periods so that their first diffraction orders were matched with these respective modes. The coupling efficiency of the first-order diffraction is dependent on the grating duty cycle, which was kept the same for all three gratings. As a result, we now have a method to selectively excite waveguide modes with decay lengths of 19 nm, 25 nm, and 39 nm.

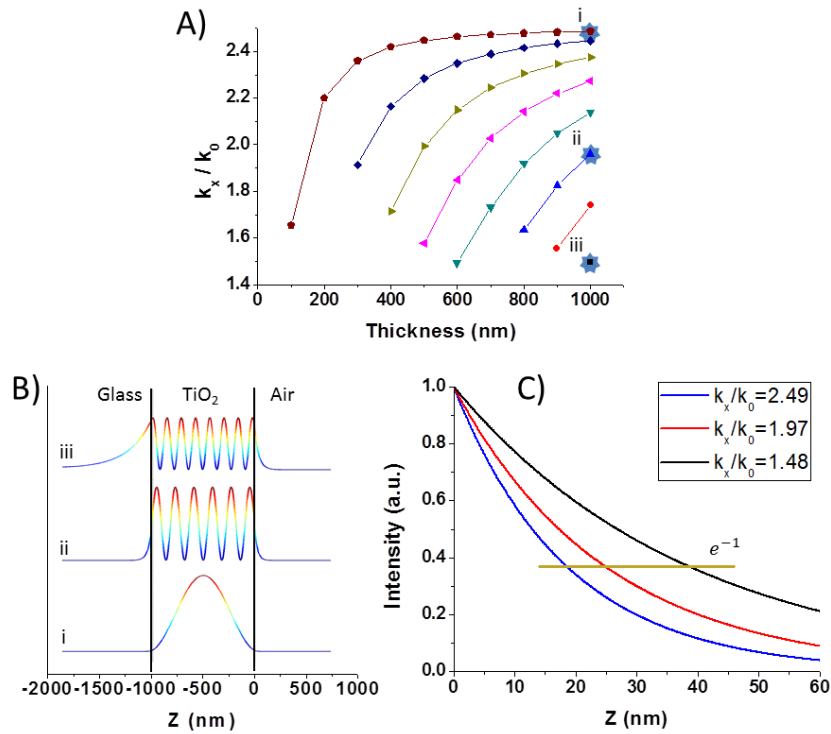


Fig. 2. A) The waveguide modes supported by different thicknesses of TiO₂ on glass. The connecting lines trace the evolution of the modes as the thickness is varied. B) The intensity distribution in- and outside TiO₂ layer of the three highlighted modes in Fig. 2(a). C) Intensity decay curve in the Z direction (perpendicular to the surface of the TiO₂ layer). The three calculated decay lengths (defined by the distance where the power decays by a factor of e^{-1}) are 19 nm, 25 nm and 39 nm.

2.2. Sample fabrication and characterization

The sample was fabricated by conventional clean room processes including electron-beam (e-beam) lithography and thin film depositions. A glass wafer was first cleaned with Piranha solution and deionized (DI) water, then spin-coated with a 200 nm thick PMMA layer (495 A2). Then we used e-beam lithography to generate the three grating patterns with periods of 214 nm, 270 nm, and 359 nm at the same duty cycle, which match the supported modes at $k_x/k_0 = 2.49$, 1.97 and 1.48 respectively. Afterwards, the patterns were transferred to the glass by dry etching of reactive-ion etching (RIE, Plus 80, Oxford Ins.) to a depth of about 50 nm. After that, we used e-beam deposition to fill the concave grating with 50 nm Au and lift-off the photoresist (Fig. 3(a)). The final 1 μ m thick TiO₂ waveguide layer was deposited by magnetron sputtering (AJA, RF).

To characterize the decay lengths of the TIRF setup, we used fluorescent beads deposited on the imaging area. The 40 nm fluorescent beads, which had excitation and emission wavelengths of 540 nm and 560 nm (F-8792 InvitrogenTM), were diluted to a concentration of about 3.4e3 particles/mL in DI water. Then we dropped 2 μ L of the nano-bead solution directly on the sample and let it dry naturally. Afterwards, the sample with fluorescent beads was rinsed with DI water, which will wash away impurities and suspended fluorescent and leave only stable beads, and the the sample is dried again under N₂.

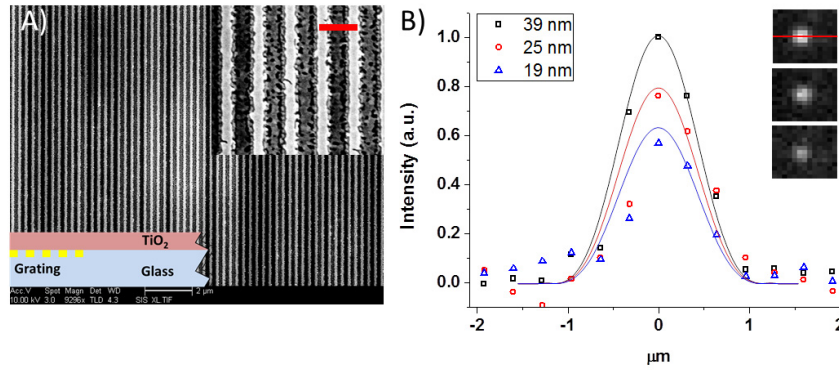


Fig. 3. A) A SEM image of the gold grating embedded in the glass layer. The scale bar is 300 nm. The left bottom inset figure shows the schematic of the grating cross-section. B) Cross-section intensities of a fluorescent nanoparticle (40 nm diameter), illuminated by evanescent waves with decay lengths of 39 nm, 25 nm and 19 nm. The experimental images are shown on the right respectively, from top to bottom. The dots display the experimental results, with the solid line showing the simulation fitting. The whole cross-section (red line) is 4160 nm.

After the preparation described above, we placed the sample face up on the stage of the upright microscope with a Carl Zeiss objective (50X, N.A. 0.55) and a Newton CCD detector (iXon3 897 Andor Corp, $16 \times 16 \mu\text{m}$ pixel size). Due to the total internal reflection, no excitation light will be transmitted through the collection objective, and therefore a fluorescence filter is unnecessary. The excitation laser (532 nm CW, BOSL-532-3, Brighten Optics) is positioned on the bottom side of the sample and illuminates the different periodic coupling gratings in succession at a normally incident angle via a series of movable mirrors and stages. The beam has a power of 50 mW at the grating interface, and with a coupling efficiency of 17.6% (calculated using the Fourier transform), we estimate that 8.8 mW is coupled into the waveguide. At the same time, we focus on one single bead and capture its image in the CCD detector (Fig. 3(b) inset).

The cross sectional intensities of a single nano-bead are shown in Fig. 3(b). The dots are the normalized intensities taken from the image cross-section at different decay lengths. All three coupling gratings were fabricated with the same duty cycle in order to keep the coupling efficiency constant. The response of the fluorescence will be linearly dependent on the local optical power, and therefore, changes in the decay length of the waveguide can be estimated by the cross-sectional intensity of the diffraction-limited single particle fluorescent image.

In order to generate the predicted intensity of the fluorescent beads (Fig. 3(b)), we use the following estimation method: The electric field intensity above the interface of total internal reflection can be expressed as: $I(z) = I_0 \exp(-2k_0 z \sqrt{\alpha^2 - 1})$. We then expect a captured image from a fluorescent particle to follow the form: $\text{Image}(x, y) = \int [I(z) \cdot \phi(x, y, z)] * P(x, y) dz$, where $\phi(x, y, z)$ is the function that describes the volume of the fluorescent particle, and $P(x, y)$ is the point spread function (PSF) of the imaging system. For a diffraction-limited optical system, the PSF of a microscope objective can be modeled as the diffraction pattern of a circular aperture (or Airy disk) following the form $I_0(2J_1(r)/r)^2$, where J_1 is the first-order Bessel function of the first kind, and r is the distance from the center of the Airy disk scaled such as the first order diffraction ring lies at the distance $d = 0.61\lambda/NA$, where λ is the wavelength of the captured light and NA is the numerical aperture of the microscope objective. Finally, all the

intensity curves were normalized to the highest values of the image with 39 nm decay length, to compare them to experimental results. In Fig. 3(b), these calculated intensities are plotted against experimental measurements. Here, we can see that the measured fluorescence profiles for the beads match the calculated profiles for different decay lengths, and these calculated profiles correlate to the experimentally observed particles, which suggests that the waveguide couplers are behaving as predicted.

2.3. Demonstration of biological imaging

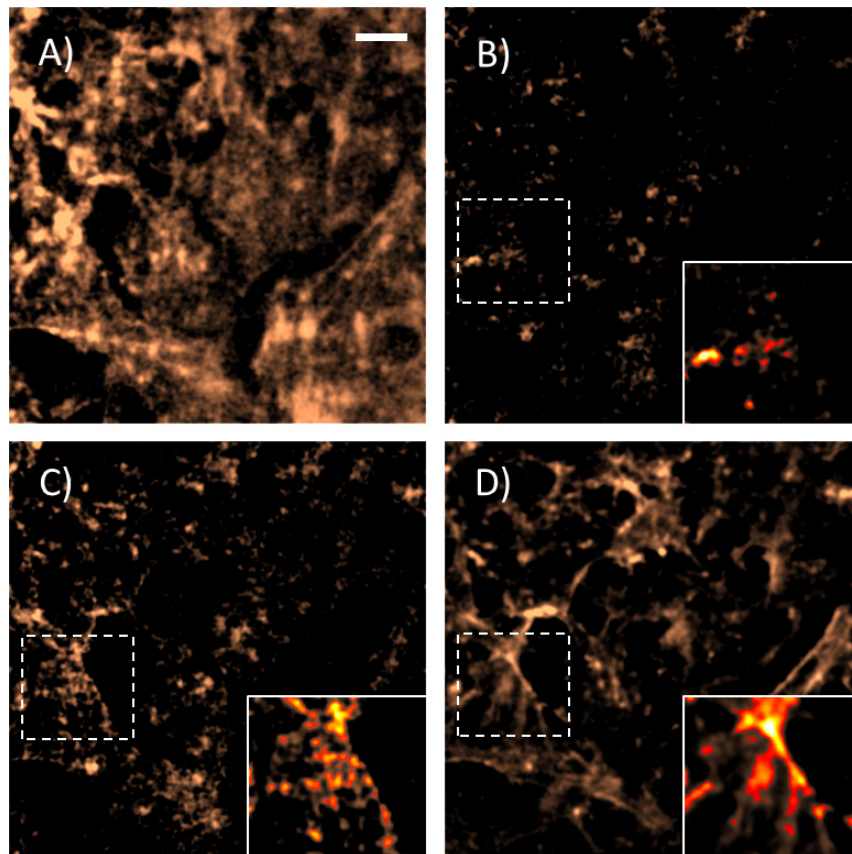


Fig. 4. Images of rhodamine phalloidin stained F-actin in HeLa cells cultured on the TiO_2 substrate. A) Direct LED illumination. B), C) and D) Evanescent wave illumination, with decay lengths of 19 nm, 25 nm and 39 nm respectively. The scale bar is 4 μm .

After confirming that we were able to adjust the decay length through grating selection, we wanted to demonstrate the imaging performance on a biological sample. For this, we chose to use HeLa cells, which were cultured on TiO_2 covered substrate in Dulbecco's Modified Eagle's Medium (Sigma) supplemented with 10% fetal bovine serum and incubated in 10% CO_2 at 37°C. Cells were fixed with 2% paraformaldehyde (in PBS) for 15 min, washed three times with PBS, and then permeabilized for 30 min with block solution (PBS containing 0.1% Triton X-100, 3% bovine serum albumin, 2% donkey serum, and 0.05 M glycine). F-Actin was labeled using Molecular Probes® rhodamine phalloidin (Ex/Em:540/565). The substrate with fixed cells was directly immersed in 10 mL PBS solution mixed with 250 μL (6.6 μM)

rhodamine phalloidin in methanolic stock solution. After 30 min at room temperature, the substrate was quickly washed with PBS three times, and then the cells were dried with N_2 . The following image process is similar to the fluorescent nanoparticles experiment, in which the green laser successively hits the different gratings, and the resulting evanescent waves illuminate the cell attached on top of the TiO_2 layer. Figure 4(a) shows the original green LED (M530L2 Thorlabs) image in reflection mode through a dichroic beam splitter (FF562-Di03-25x36, Semrock), exciting band pass filter (FF01-543/22-25, Semrock) and emission band pass filter (FF01-593/40-25, Semrock).

Unlike Fig. 4(a), which displays most of the fluorescent info throughout the cell, Figs. 4(b)–4(d) selectively excites a TIRF image at various layers with penetration depths at 19 nm, 25 nm and 38 nm. In Fig. 4(b), there are very few visible structures illuminated by the short decay length. The inset figure with highlight clearly shows some individual fluorescent dye particles close to the surface. In Fig. 4(c), some of the fluorescent dye suspended in the cell as well as the blurred edges of the cell becomes visible when the decay length increases to 25 nm. For emphasis, we highlight some clusters with higher intensities (inset figure). By contrast, in Fig. 4(d) both the edge of the cell and the F-actins in the cell can be easily distinguished, as they are farther away from the sample surface. It is important to note that the purpose of these images was to demonstrate depth control in our system, so we did not attempt to identify the visible structures. These results demonstrate that the ability to control decay length can be used to discern structures with very high resolution in the z direction.

3. Conclusions

In summary, by using multiple diffraction gratings coupled to a high-index TiO_2 layer, we were able to achieve a tunable decay length between 20 and 40 nanometers in an internally reflected waveguide mode. Fluorescent nano-beads were illuminated with the various grating couplers, and their fluorescence profiles were compared to simulated profiles in order to estimate their decay lengths. Finally, we demonstrated the application of our TIRF technique in an F-actin labeled HeLa cell, and showed that the variation of decay length makes it possible to distinguish unique structures at various distances from the surface. By contrast, conventional TIRF microscopy is limited to a single decay length, and is not able to access this additional z-direction information. Therefore, the capabilities of our compact TIRF technique will be valuable for various systems and lab-on-a-chip applications, such as stretched DNA and protein detection, where information exists in multiple depth planes close to the surface.

Acknowledgment

This research is partially funded by NSF-ECCS under Grant 0969405.